

## Article

# Hyperpolarized $^{13}\text{C}$ Magnetic Resonance Spectroscopic Imaging of Pyruvate Metabolism in Murine Breast Cancer Models of Different Metastatic Potential

Erin B. Macdonald <sup>1,†</sup>, Paul Begovatz <sup>1,†</sup>, Gregory P. Barton <sup>1</sup> , Sarah Erickson-Bhatt <sup>2,3,4</sup>, David R. Inman <sup>4</sup>, Benjamin L. Cox <sup>1,2,3</sup>, Kevin W. Eliceiri <sup>1,2,3,5,6</sup> , Roberta M. Strigel <sup>1,6,7</sup>, Suzanne M. Ponik <sup>4,6,†</sup>  and Sean B. Fain <sup>1,5,6,7,\*</sup> 

- <sup>1</sup> Department of Medical Physics, University of Wisconsin-Madison, 1111 Highland Ave., Madison, WI 53705, USA; erin.beth.macdonald@gmail.com (E.B.M.); begovatz@wisc.edu (P.B.); gregory.barton@uwsouthwestern.edu (G.P.B.); bcox1@wisc.edu (B.L.C.); eliceiri@wisc.edu (K.W.E.); rstrigel@uwhealth.org (R.M.S.)
- <sup>2</sup> Morgridge Institute for Research, 330 N. Orchard St., Madison, WI 53715, USA; sarah.e.bhatt@gmail.com
- <sup>3</sup> Laboratory for Optical and Computational Instrumentation, University of Wisconsin-Madison, Madison, WI 53706, USA
- <sup>4</sup> Department of Cell and Regenerative Biology, University of Wisconsin-Madison, 1111 Highland Ave., Madison, WI 53705, USA; drinman@facstaff.wisc.edu (D.R.I.); ponik@wisc.edu (S.M.P.)
- <sup>5</sup> Department of Biomedical Engineering, University of Wisconsin-Madison, 1415 Engineering Dr., Madison, WI 53706, USA
- <sup>6</sup> Carbone Cancer Center, University of Wisconsin-Madison, 600 Highland Ave., Madison, WI 53705, USA
- <sup>7</sup> Department of Radiology, University of Wisconsin-Madison, 600 Highland Ave., Madison, WI 53792, USA
- \* Correspondence: sfain@wisc.edu; Tel.: +1-608-263-0090
- † These authors contributed equally to this work.



**Citation:** Macdonald, E.B.; Begovatz, P.; Barton, G.P.; Erickson-Bhatt, S.; Inman, D.R.; Cox, B.L.; Eliceiri, K.W.; Strigel, R.M.; Ponik, S.M.; Fain, S.B. Hyperpolarized  $^{13}\text{C}$  Magnetic Resonance Spectroscopic Imaging of Pyruvate Metabolism in Murine Breast Cancer Models of Different Metastatic Potential. *Metabolites* **2021**, *11*, 274. <https://doi.org/10.3390/metabo11050274>

Academic Editors: Andre F. Martins and Myriam M. Chaumeil

Received: 19 February 2021

Accepted: 21 April 2021

Published: 27 April 2021

**Publisher's Note:** MDPI stays neutral with regard to jurisdictional claims in published maps and institutional affiliations.



**Copyright:** © 2021 by the authors. Licensee MDPI, Basel, Switzerland. This article is an open access article distributed under the terms and conditions of the Creative Commons Attribution (CC BY) license (<https://creativecommons.org/licenses/by/4.0/>).

**Abstract:** This study uses dynamic hyperpolarized [ $1\text{-}^{13}\text{C}$ ]pyruvate magnetic resonance spectroscopic imaging (MRSI) to estimate differences in glycolytic metabolism between highly metastatic (4T1,  $n = 7$ ) and metastatically dormant (4T07,  $n = 7$ ) murine breast cancer models. The apparent conversion rate of pyruvate-to-lactate ( $k_{\text{PL}}$ ) and lactate-to-pyruvate area-under-the-curve ratio ( $\text{AUC}_{\text{L/P}}$ ) were estimated from the metabolite images and compared with biochemical metabolic measures and immunohistochemistry (IHC). A non-significant trend of increasing  $k_{\text{PL}}$  ( $p = 0.17$ ) and  $\text{AUC}_{\text{L/P}}$  ( $p = 0.11$ ) from 4T07 to 4T1 tumors was observed. No significant differences in tumor IHC lactate dehydrogenase-A (LDHA), monocarboxylate transporter-1 (MCT1), cluster of differentiation 31 (CD31), and hypoxia inducible factor- $\alpha$  (HIF-1 $\alpha$ ), tumor lactate-dehydrogenase (LDH) activity, or blood lactate or glucose levels were found between the two tumor lines. However,  $\text{AUC}_{\text{L/P}}$  was significantly correlated with tumor LDH activity ( $\rho_{\text{spearman}} = 0.621$ ,  $p = 0.027$ ) and blood glucose levels ( $\rho_{\text{spearman}} = -0.474$ ,  $p = 0.042$ ).  $k_{\text{PL}}$  displayed a similar, non-significant trend for LDH activity ( $\rho_{\text{spearman}} = 0.480$ ,  $p = 0.114$ ) and blood glucose levels ( $\rho_{\text{spearman}} = -0.414$ ,  $p = 0.088$ ). Neither  $k_{\text{PL}}$  nor  $\text{AUC}_{\text{L/P}}$  were significantly correlated with blood lactate levels or tumor LDHA or MCT1. The significant positive correlation between  $\text{AUC}_{\text{L/P}}$  and tumor LDH activity indicates the potential of  $\text{AUC}_{\text{L/P}}$  as a biomarker of glycolytic metabolism in breast cancer models. However, the lack of a significant difference between in vivo tumor metabolism for the two models suggest similar pyruvate-to-lactate conversion despite differing metastatic potential.

**Keywords:** breast cancer; metastatic potential; metabolism; MRSI; hyperpolarized; carbon-13; repeatability

## 1. Introduction

Breast cancer is the most common cancer diagnosis in women worldwide. This disease is responsible for the second most cancer-related deaths for women in developed countries and the most cancer-related deaths for women in developing countries [1]. Treatment of

metastatic disease is still challenging in-part because tumor cells can remain dormant at distal sites for years to decades before emerging into overt metastatic outgrowth [2]. There is a critical need to identify and distinguish tumors that are highly metastatic from those that are metastatically dormant.

One hallmark of cancer is dysregulated energy metabolism [3]. As early as 1924, Otto Warburg observed that tumors and highly proliferative tissues exhibited upregulated glycolysis with increased pyruvate-to-lactate conversion compared with healthy normal tissues, independent of local oxygen availability [4]. While committing pyruvate to oxidative phosphorylation constitutes a more efficient means of energy metabolism, in cancer the lactate-dehydrogenase (LDH)-mediated conversion of pyruvate to lactate is hypothesized to enable production of glycolytic intermediates useful for building the macromolecules required for cell proliferation. Higher glycolytic rates may indicate more highly proliferative and aggressive tumors. Indeed, tumor lactate levels have been significantly positively correlated with the development of distant metastasis despite there being different lactate levels in tumors of the same grade and stage [5]. These results suggest that tumor lactate production may be an important biomarker for breast cancer aggressiveness and propensity to metastasize.

A promising technique for interrogating real-time in vivo metabolism is hyperpolarized  $^{13}\text{C}$  magnetic resonance spectroscopic imaging (MRSI). With this technique,  $^{13}\text{C}$ -labeled molecules of biological interest are exogenously hyperpolarized using dynamic nuclear polarization (DNP) to increase their MR signal from levels undetectable in a practical imaging timeframe to over 10,000-fold times higher [6]. The hyperpolarized  $^{13}\text{C}$ -labeled substrate is intravenously injected for imaging tumor metabolism in vivo, enabling the hyperpolarized  $^{13}\text{C}$  label to be observed as it is converted to downstream metabolites, each of which resonates at its own characteristic chemical shift frequency uniquely detected by the MR scanner [6].

Due to its important role in energy metabolism and amenability to hyperpolarization,  $[1-^{13}\text{C}]$ pyruvate is the most commonly used substrate in hyperpolarized  $^{13}\text{C}$  magnetic resonance spectroscopy (MRS) and MRSI. Some of the earliest applications of hyperpolarized  $^{13}\text{C}$  MRS/MRSI exploited hyperpolarized  $[1-^{13}\text{C}]$ pyruvate to monitor its LDH-mediated conversion to  $[1-^{13}\text{C}]$ lactate in cancers, where glycolytic rates were expected to be high [7,8]. Hyperpolarized  $^{13}\text{C}$  MRS/MRSI has specific applications in breast cancer but with sometimes unexpected results. For example, Xu et al. explored differences in the apparent conversion rate of pyruvate-to-lactate ( $k_{\text{PL}}$ ) in mouse xenograft models of breast cancer with different levels of aggressiveness and found that more indolent tumors exhibited higher  $k_{\text{PL}}$  values, contrary to the conventional model of upregulated aerobic glycolysis predicted by the Warburg hypothesis [9,10]. In contrast, Ward et al. demonstrated the sensitivity of hyperpolarized pyruvate-to-lactate conversion to LDH modulation by inhibiting phosphoinositide 3-kinases (PI3K), a key enzyme implicated in cancer development and involved in regulating LDH concentrations [11]. An MYC-driven breast cancer tumor model was used to demonstrate decreased pyruvate-to-lactate conversion with reduced MYC-driven tumor progression and increased pyruvate-to-lactate conversion with cancer recurrence [12]. Despite the mechanistic complexity of breast cancers, the promise of hyperpolarized  $[1-^{13}\text{C}]$ pyruvate MRS/MRSI has even fostered its initial translation into patients with invasive breast cancer [13] where the lactate/pyruvate ratio was positively and strongly correlated to monocarboxylate transporter 1 (MCT1) RNA expression suggesting cell membrane MCT1, rather than LDH activity, is rate-limiting in invasive breast cancers.

Dormant tumor cells, in other words, tumors that seed cells to distant sites but fail to form metastatic nodules, have been shown to disseminate at early tumor stages due to acquiring a highly motile, slowly proliferating phenotype [14]. While the mechanisms by which tumor cells acquire a dormant phenotype is not yet fully understood, markers of dormancy can be induced by hypoxia and dormant cells are characterized by reduced expression of the glucose transporter, Glut-1, and a shift in signaling from extracellular signal-related kinase (ERK) to p-38. However, in vitro studies using models of dormant tu-

mor cells with the Seahorse flux analyzer method suggest the utilization of glucose through glycolysis is not significantly altered compared to metastatically aggressive cell lines [15]. In total, these characteristics suggest the dormant subpopulation of tumor cells might be identified by a unique metabolic signature stemming from tumor microenvironmental conditions *in vivo*, including possibly altered glycolysis due to local hypoxia [5]. However, the utility of hyperpolarized [1-<sup>13</sup>C]pyruvate MRSI as a prognostic marker to differentiate between breast cancers that are highly metastatic and those that are metastatic but dormant has not been directly explored.

In this work, we investigate the use of hyperpolarized [1-<sup>13</sup>C]pyruvate MRSI to differentiate between murine breast tumor xenografts of highly metastatic and metastatically dormant cells. Specifically, *in vivo* experiments were performed in highly metastatic 4T1 murine breast tumors and metastatically dormant 4T07 murine breast tumors that seed cells to the lungs and liver but do not form metastatic nodules. Dynamic hyperpolarized <sup>13</sup>C MRSI data were used to estimate two measures of pyruvate to lactate conversion in these tumor models: (1) the apparent pyruvate-to-lactate conversion rate ( $k_{PL}$ ) and (2) the area-under-the-curve ratio of lactate-to-pyruvate ( $AUC_{L/P}$ ), a model-free metric known to be proportional to  $k_{PL}$  [16]. In exploratory studies, both  $k_{PL}$  and  $AUC_{L/P}$  were compared to independent measures of tumor LDH concentrations, immunohistochemistry (IHC), and serum lactate and glucose levels to study possible mechanisms mediating pyruvate-to-lactate conversion in these cell lines. Finally, a subset of mice underwent repeated testing 48 h later to gain insight into the variability of  $k_{PL}$  and  $AUC_{L/P}$  measures of pyruvate-to-lactate metabolism.

## 2. Results

### 2.1. Tumor Size

Estimated volumes and measured masses for both 4T07 and 4T1 tumor models at the last imaging time point are summarized in Table 1. The mean tumor volumes and masses were in good agreement between the metastatic dormant 4T07 and highly metastatic 4T1 tumor models. Variability in the 4T07 tumor dimensions was higher due to more variable growth rates compared to more rapidly proliferating 4T1 tumors.

**Table 1.** Estimated tumor volumes and measured tumor masses for both metastatic dormant 4T07 and metastatic proliferative 4T1 tumor lines.

Tumor Model	<i>n</i>	Volume (mm <sup>3</sup> ) Mean ± SD	Mass (mg) Mean ± SD	Days Post-Inoculation Mean ± SD
4T07	7	184 ± 178	163 ± 145	21 ± 8
4T1	7	195 ± 84	150 ± 58	12 ± 1

### 2.2. Immunohistochemistry and Biochemical Analysis

Analysis of tumor tissue using immunohistochemistry revealed no differences in the presence of LDHA ( $p = 0.52$ ), or the MCT1 transporter ( $p = 0.43$ ) between metastatic 4T1 and metastatic-dormant 4T07 tumors (Figure 1). Furthermore, the presence of hypoxia inducible factor (HIF)-1 $\alpha$  was investigated in order to identify changes in tumor lactate production which could be driven by hypoxia within the tumor microenvironment, rather than the anaerobic glycolysis; however, HIF-1 $\alpha$  expression was also found to be equal between the tumor types ( $p = 0.52$ ). Lastly, the area of CD31 immunohistochemistry was quantified to evaluate any differences in the presence of endothelial cells as an indicator of tumor vascularization. We found no change in CD31 area per tumor ( $p = 0.18$ ), suggesting that vascularization and thus the delivery of hyperpolarized [1-<sup>13</sup>C]pyruvate was similar for all tumors. Mean IHC intensities are summarized in Figure 1 and Table 2 and representative images of each marker are shown in Appendix A.

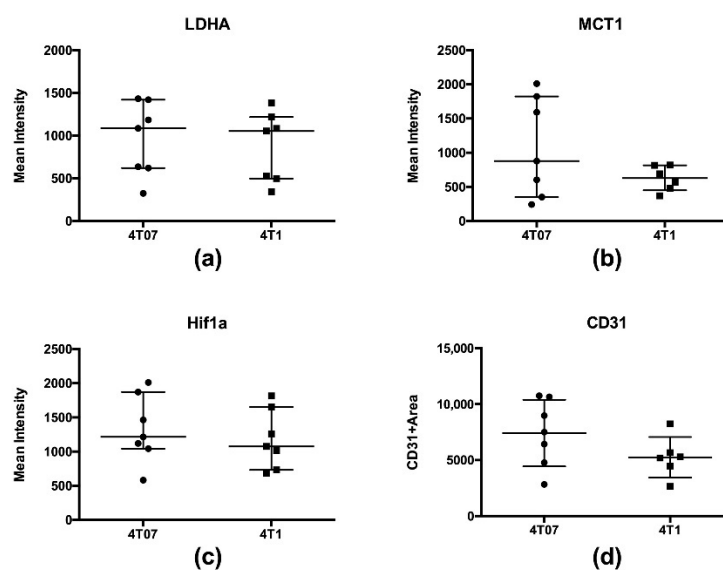


**Figure 1.** Comparison of immunohistochemistry results between 4T07 and 4T1 tumors: (a) LDHA; (b) MCT1 transporter; (c) HIF-1 $\alpha$ ; (d) and presence of endothelial cells via CD31. Error bars represent the median, 25th, and 75th percentiles.

**Table 2.** Statistical results comparing imaging, biochemical, and immunohistochemical metabolic measures between 4T07 and 4T1 tumor models.

Metabolic Measure	4T07		4T1		Unpaired <i>t</i> -Test
	Mean $\pm$ SD	# Samples	Mean $\pm$ SD	# Samples	
$k_{PL}$ ( $s^{-1}$ )	0.033 $\pm$ 0.015	7	0.052 $\pm$ 0.027	6	$p = 0.17$
AUC <sub>L/P</sub>	0.81 $\pm$ 0.15	7	1.08 $\pm$ 0.38	7	$p = 0.11$
Blood lactate (mM)	4.7 $\pm$ 0.9	6	4.3 $\pm$ 0.7	7	$p = 0.45$
Blood glucose (mg/dL)	228 $\pm$ 33	6	194 $\pm$ 43	7	$p = 0.14$
Tumor LDH (nmol/min/mL/mg)	535 $\pm$ 128	6	588 $\pm$ 102	7	$p = 0.44$
Tumor LDHA (mean intensity)	958 $\pm$ 433	7	872 $\pm$ 408	7	$p = 0.52$
Tumor MCT1 (mean intensity)	1071 $\pm$ 729	7	623 $\pm$ 184	6	$p = 0.18$
Tumor HIF-1 $\alpha$ (mean intensity)	1329 $\pm$ 496	7	1176 $\pm$ 432	7	$p = 0.52$
Tumor CD31 (CD31 + area)	7422 $\pm$ 2973	7	5253 $\pm$ 1814	6	$p = 0.43$

Number of samples (# samples), area under the curve (AUC), lactate dehydrogenase-A (LDHA), monocarboxylate transporter-1 (MCT1), cluster of differentiation 31 (CD31), and hypoxia inducible factor- $\alpha$  (HIF-1 $\alpha$ ).

No significant differences in tumor LDH activity, or blood lactate or glucose levels, were found between the two tumor lines (Table 2). Blood glucose levels did not significantly differ in mice bearing metastatic dormant 4T07 tumors compared to mice with more aggressive metastatic 4T1 tumors ( $p = 0.14$ ).

### 2.3. Metabolic Imaging

Representative hyperpolarized [ $1-^{13}C$ ]pyruvate and [ $1-^{13}C$ ]lactate AUC images for each tumor model are displayed in Figure 2 along with their corresponding metabolite time courses and kinetic modeling fits. Boxplots of the resulting distribution of  $k_{PL}$  and AUC<sub>L/P</sub> estimates for each tumor model are given in Figure 3. Mean metabolic imaging measures are summarized in Table 2, above. No significant differences in either metabolic imaging metric were found between the metastatic dormant 4T07 and metastatic 4T1 primary tumors. However, there is a trend of increasing  $k_{PL}$  ( $p = 0.17$ ) and AUC<sub>L/P</sub> ( $p = 0.11$ ) for metastatic 4T1 tumors compared to metastatic dormant 4T07 tumors.

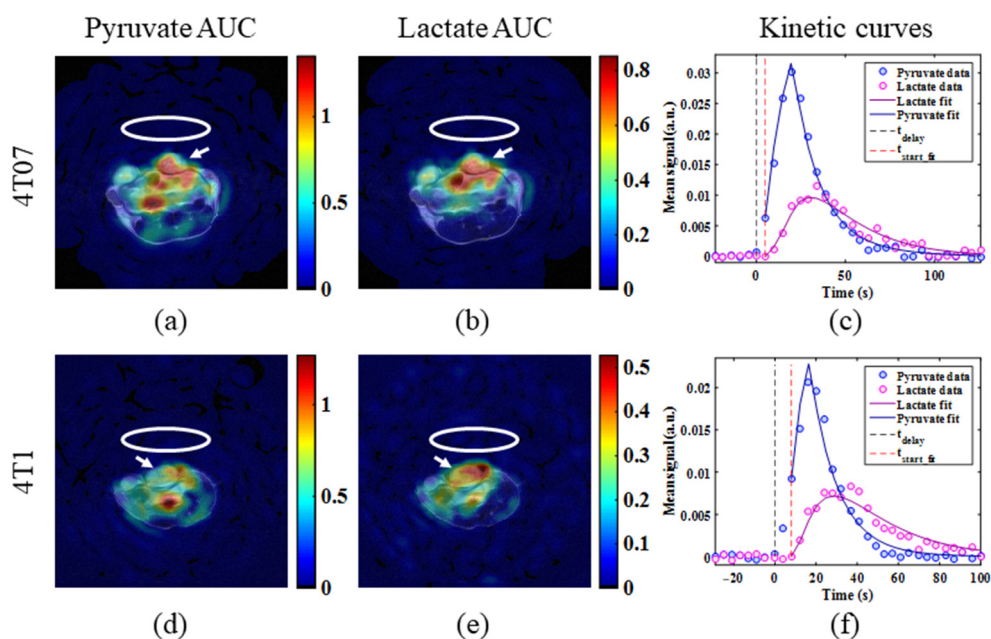


**Figure 2.** Representative hyperpolarized (a,d)  $[1-^{13}\text{C}]$ pyruvate and (b,e)  $[1-^{13}\text{C}]$ lactate AUC images (color) overlaid on  $T_2$ -weighted anatomical reference images (grayscale) for mice bearing (a,b) metastatic dormant 4T07 tumors and (d,e) more aggressive, metastatic 4T1 tumors. The approximate  $^{13}\text{C}$  surface coil location and targeted tumor for imaging are indicated by white ovals and white arrows, respectively. The corresponding pyruvate and lactate metabolite time courses from the targeted imaging tumor are displayed for the (c) 4T07 and (f) 4T1 breast cancer models along with the fitted curves. The time of hyperpolarized  $[1-^{13}\text{C}]$ pyruvate injection is indicated by  $t_{\text{delay}}$  and the first time point used for kinetic modeling is labeled with  $t_{\text{start\_fit}}$ .

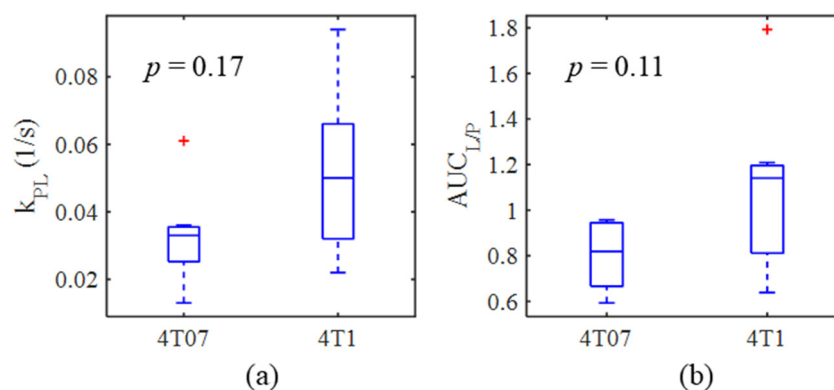


**Figure 3.** Boxplots comparing the distribution of (a)  $k_{\text{PL}}$  and (b)  $\text{AUC}_{\text{L/P}}$  between metastatic dormant 4T07 and highly metastatic 4T1 tumor models. Box plots represent the median with upper and lower limits representing the 25th and 75th percentiles, whiskers the minimum and maximum, and red crosses the outliers.

#### 2.4. Correlations between Metabolic Measures

All Spearman correlation test results are summarized in Table 3.  $\text{AUC}_{\text{L/P}}$  was moderately correlated to  $k_{\text{PL}}$  ( $\rho_{\text{spearman}} = 0.67$ ,  $p = 0.002$ ) as expected (Figure A2). The  $k_{\text{PL}}$  measure was moderately repeatable with a coefficient of repeatability ( $\text{CR } k_{\text{PL}} = 0.04 \text{ s}^{-1}$ ) and negligible bias (Figure A3 and Table A1).  $\text{AUC}_{\text{L/P}}$  was somewhat less repeatable ( $\text{CR } \text{AUC} = 1.2$ ), with a larger coefficient of variation than  $k_{\text{PL}}$  ( $\text{COV: } \text{AUC} = 0.29$  vs.  $k_{\text{PL}} = 0.23$ ), but also showed negligible bias and no significant difference between time points.

**Table 3.** Spearman correlation results.

Comparison	Tumor Models Included	Time Points Included <sup>a</sup>	$\rho_{\text{spearman}}$	$p$ -Value
$k_{\text{PL}}$ vs. tumor LDH	pooled 4T1 and 4T07	final	0.480	0.114
$k_{\text{PL}}$ vs. blood lactate	pooled 4T1 and 4T07	all	−0.181	0.472
$k_{\text{PL}}$ vs. blood glucose	pooled 4T1 and 4T07	all	−0.414	0.088
$k_{\text{PL}}$ vs. tumor LDHA	pooled 4T1 and 4T07	final	0.459	0.115
$k_{\text{PL}}$ vs. tumor MCT1	pooled 4T1 and 4T07	final	−0.403	0.172
$k_{\text{PL}}$ vs. tumor HIF-1 $\alpha$	pooled 4T1 and 4T07	final	−0.163	0.593
$k_{\text{PL}}$ vs. tumor CD31	pooled 4T1 and 4T07	final	−0.233	0.443
$k_{\text{PL}}$ vs. tumor volume	pooled 4T1 and 4T07	final	−0.201	0.511
AUC <sub>L/P</sub> vs. tumor LDH	pooled 4T1 and 4T07	final	0.621	0.027
AUC <sub>L/P</sub> vs. blood lactate	pooled 4T1 and 4T07	all	−0.067	0.786
AUC <sub>L/P</sub> vs. blood glucose	pooled 4T1 and 4T07	all	−0.474	0.042
AUC <sub>L/P</sub> vs. tumor LDHA	pooled 4T1 and 4T07	final	−0.057	0.844
AUC <sub>L/P</sub> vs. tumor MCT1	pooled 4T1 and 4T07	final	−0.479	0.083
AUC <sub>L/P</sub> vs. tumor HIF-1 $\alpha$	pooled 4T1 and 4T07	final	−0.275	0.342
AUC <sub>L/P</sub> vs. tumor CD31	pooled 4T1 and 4T07	final	0.416	0.139
AUC <sub>L/P</sub> vs. tumor CD31	pooled 4T1 and 4T07	final	−0.002	1.000
AUC <sub>L/P</sub> vs. $k_{\text{PL}}$	pooled 4T1 and 4T07	all	0.665	0.002
LDHA vs. tumor volume	pooled 4T1 and 4T07	final	−0.284	0.325
MCT1 vs. tumor volume	pooled 4T1 and 4T07	final	0.351	0.239
HIF-1 $\alpha$ vs. tumor volume	pooled 4T1 and 4T07	final	−0.095	0.750
CD31 vs. tumor volume	pooled 4T1 and 4T07	final	−0.024	0.940
LDHA vs. LDH activity	pooled 4T1 and 4T07	final	0.066	0.835

<sup>a</sup> “Time points included” refers to the imaging time point data used from each mouse to perform the correlation test. “final” refers to the final imaging experiment for each mouse, some of which had repeat experiments. “all” refers to all imaging experiments, including the repeat experiments.

Importantly, AUC<sub>L/P</sub> was significantly correlated ( $\rho_{\text{spearman}} = 0.62$ ,  $p = 0.027$ ) with measured tumor LDH activity (Figure 4).  $k_{\text{PL}}$  displayed a similar trend of increasing value with increased tumor LDH activity, but the results did not reach significance ( $\rho_{\text{spearman}} = 0.48$ ,  $p = 0.114$ ).

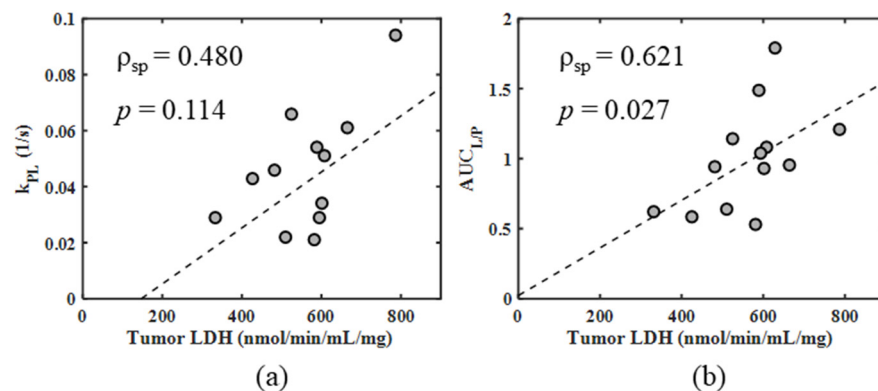


**Figure 4.** Spearman correlation plots comparing (a)  $k_{\text{PL}}$  and (b) AUC<sub>L/P</sub> with tumor LDH activity. Spearman correlation coefficients ( $\rho_{\text{sp}}$ ) and  $p$ -values are listed on the plots.

The correlation plots comparing imaging measures of metabolism with blood lactate and glucose levels are displayed in Figure 5. Neither  $k_{\text{PL}}$  nor AUC<sub>L/P</sub> had a significant correlation with blood lactate levels. However, AUC<sub>L/P</sub> was significantly negatively correlated with blood glucose levels ( $\rho_{\text{spearman}} = -0.47$ ,  $p = 0.042$ ) and  $k_{\text{PL}}$  displayed a similar trend of decreasing value with increased blood glucose ( $\rho_{\text{spearman}} = -0.41$ ,  $p = 0.088$ ).

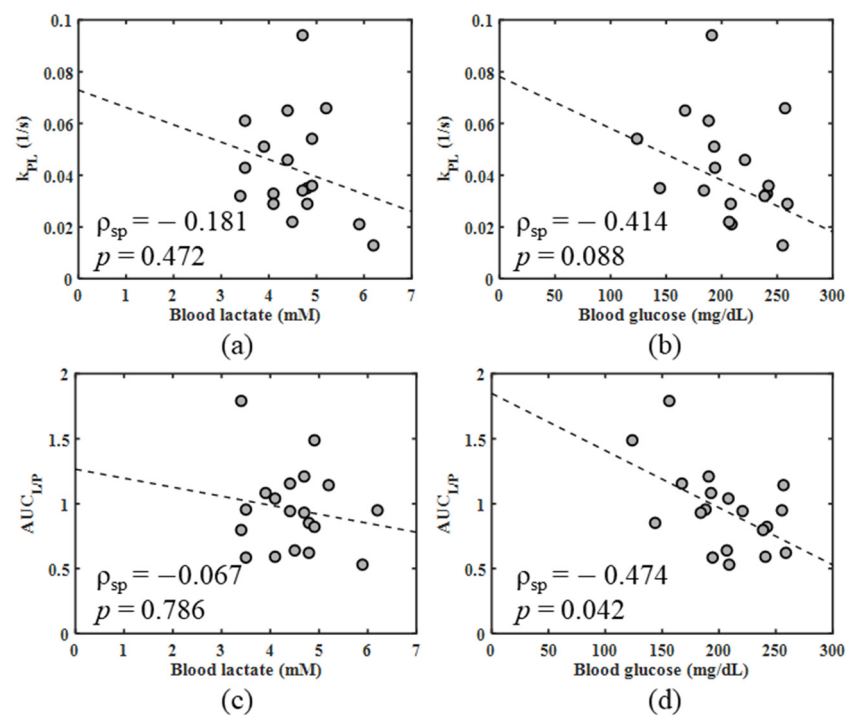


**Figure 5.** Spearman correlation plots comparing  $k_{PL}$  with blood (a) lactate and (b) glucose levels, and  $AUC_{L/P}$  with blood (c) lactate and (d) glucose levels. Spearman correlation coefficients ( $\rho_{sp}$ ) and  $p$ -values are listed on the plots.

### 3. Discussion

Most breast cancer deaths are the result of metastatic disease rather than the primary tumor with many metastatic breast cancer patients succumbing to lactic acidosis [17], suggesting altered metabolism may play an important role in patient outcome. Indeed, upregulated glycolysis with increased pyruvate-to-lactate has been widely observed in tumors [4,18] including breast cancer [19]. Furthermore, tumor lactate levels have been significantly positively correlated with incidence of metastasis [5]. We used dynamic hyperpolarized  $^{13}\text{C}$  MRSI to investigate in vivo differences in pyruvate-to-lactate conversion (i.e.,  $k_{PL}$  and  $AUC_{L/P}$ ) for metastatic dormant 4T07 and highly metastatic 4T1 tumors. Differences in  $k_{PL}$  and  $AUC_{L/P}$  did not reach statistical significance, suggesting similar pyruvate utilization in glycolysis for in vivo tumors, similar to in vitro findings using Seahorse flux analysis for the 4T1 and 4T07 cell lines [15]. Interestingly, there was a significant positive correlation between  $AUC_{L/P}$  and tumor LDH activity, and an observed trend towards higher  $AUC_{L/P}$  measures in the more metastatic 4T1 tumor model, but no significant differences were found in tumor LDH activity between the 4T07 and 4T1 tumors. This suggests that metastatic tumor potential is mediated by other metabolic processes such as increased glutamine metabolism [15]. Additionally, the trend of increased  $AUC_{L/P}$  and increased  $k_{PL}$  in more metastatic tumors may be influenced by other rate limiting steps in the conversion of pyruvate to lactate, such as hyperpolarized  $[1-^{13}\text{C}]$ pyruvate delivery to the tumor (i.e., perfusion) [20], hyperpolarized  $[1-^{13}\text{C}]$ pyruvate transport into the cell [19], the concentration of coenzyme nicotinamide adenine dinucleotide (NADH) [9], and the size of endogenous metabolite pools [21]. Follow-up histology and immunohistochemistry staining for microvascularity (CD31), MCT1, HIF-1 $\alpha$ , and LDHA did not differ with metastatic potential either. Furthermore, tumor LDH activity and LDHA protein expression were not significantly correlated. While this result may seem unexpected, changes in LDH activity do not necessarily depend on the expression of LDHA. LDHA activity has been shown to be regulated by Src- or Her2-mediated phosphorylation of Y10 on LDHA [22]. Future work will address the possibility that LDHA activity in 4T1 or 4T07 tumors is regulated by phosphorylation.

Another *in vivo* study found that higher perfusion-corrected uptake of a fluorescent glucose derivative was observed in the metastatic 4T1 tumors compared to metastatic dormant 4T07 tumors for the same vascular oxygenation, indicating an increased shift towards glucose uptake via GLUT1 and presumably aerobic glycolysis in the highly metastatic 4T1 tumors [23]. However, this inference is not supported by our study, possibly because the pyruvate substrate follows a different path into the cell via monocarboxylate transporters (especially MCT1) in the cell membrane [24]. Indeed, in our study MCT1 neither differed between the tumor models or correlated to  $AUC_{L/P}$  or  $k_{PL}$ , suggesting tumor LDH activity is a stronger driver of increased lactate production from the pyruvate substrate than MCT1 expression in these tumor models. This differs from recent findings in invasive human breast cancer that found stronger associations between pyruvate to lactate conversion and MCT1 expression than with LDH activity [19]. In this work,  $AUC_{L/P}$  was found to be significantly positively correlated with tumor LDH activity while  $k_{PL}$  displayed a similar, although non-significant, positive relationship. The stronger correlation between  $AUC_{L/P}$  and tumor LDH activity is likely attributable, at least in part, to its calculation from higher signal-to-noise ratio (SNR) data, with hyperpolarized  $^{13}C$  metabolite signals integrated over time as opposed to the time-resolved data points used for fitting  $k_{PL}$ . Additionally, the goodness of fit of the kinetic model used to estimate  $k_{PL}$  depends on the choice of initial time frame with which to begin fitting, making it more susceptible to inaccuracies from noisy data than  $AUC_{L/P}$ . Furthermore, pyruvate inflow affects the shape of the metabolite time courses and can bias metabolic measures. This work employed a two-way exchange model with an additional Heaviside step function term to model pyruvate inflow and help account for its influence on the fitted rate constants [25]. However, the Heaviside step function is an imperfect approximation of true pyruvate inflow and is unlikely to fully capture the true dynamics of pyruvate infusion. This lends additional appeal to  $AUC_{L/P}$ , which is independent of both the pyruvate inflow function and the rates of pyruvate interconversion with metabolites other than lactate. Therefore, given that both  $k_{PL}$  and  $AUC_{L/P}$  are related to the same physiologic process, this work suggests  $AUC_{L/P}$  is a more sensitive biomarker of tumor LDH activity than  $k_{PL}$ .

While the present work indicates potential for  $k_{PL}$  and  $AUC_{L/P}$  from hyperpolarized  $^{13}C$  MRSI of whole tumors, both tumor models used in this study are characterized by malignant primary tumors that seed metastatic nodules to distant sites. Therefore, differences in glycolysis may be too small for us to detect in a small study such as this, suggesting assessment of complementary metabolic pathways might show more pronounced differences as a complement to glycolytic rates. Both  $AUC_{L/P}$  and  $k_{PL}$  measures of pyruvate-to-lactate conversion are almost certainly influenced by more than just LDH activity. Concentration of coenzyme NADH [9], transport of hyperpolarized  $[1-^{13}C]$ pyruvate via perfusion [20], and the size of endogenous metabolite pools [21] may all play a role in the observed metabolite dynamics.

Although upregulated glycolysis is a common feature associated with malignancy, recent works have suggested that mitochondrial oxidative phosphorylation may still be the dominant source of energy production in cancerous cells [18]. Scarcity of pyruvate substrate to fuel the tricarboxylic acid (TCA) cycle has been shown to provoke cancerous cells to use alternative sources, such as glutamine [26,27]. Furthermore, previous work by Xu et al. demonstrated that spatial patterns of increased mitochondrial redox state were predictive of tumor metastatic potential in breast cancer models, indicating mitochondrial metabolism may be more predictive of metastasis than cytosolic glycolysis alone [28]. Therefore, a more complete picture of differences in tumor metabolism between primary breast cancers of different metastatic potential may be gained by investigating the relative rates of glycolytic metabolism and oxidative phosphorylation. While the hyperpolarized  $^{13}C_1$  label on pyruvate is not transferrable to molecules in the TCA cycle,  $[2-^{13}C]$ pyruvate and  $[1,2-^{13}C]$ pyruvate have both been hyperpolarized to investigate glycolytic and mitochondrial metabolism simultaneously [29,30].  $[5-^{13}C]$ glutamine has also been successfully hyperpolarized for application in evaluating cancer metabolism [31] and may be a promis-

ing substrate for investigation in metastasis. Therefore, in addition to providing a potential biomarker for LDH-mediated conversion of pyruvate-to-lactate, hyperpolarized  $^{13}\text{C}$  MRSI offers the tools for a more comprehensive analysis of energy metabolism in breast cancer.

Finally, an unexpected trend observed in the present work was the tendency for blood glucose concentrations to be lower in the metastatic 4T1 tumor-bearing mice than the metastatic dormant 4T07 mouse models despite both sets of mice being consistently fasted for the same amount of time prior to imaging. While the direction of the association with blood glucose is at odds with ample literature demonstrating a link between blood glucose levels and increased risk of malignancy [32,33], the discrepancy may be reconciled by the fact that the tumor cells were injected into bilateral fat pads these mice as xenografts rather than occurring spontaneously. It is possible that, instead, the more aggressive and metastatic 4T1 tumors exert a higher energy demand on the systemic physiology than the metastatic dormant 4T07 tumors resulting in a hypoglycemic effect [34,35]. The energy demand from the rapidly growing 4T1 tumors may be further exacerbated by the burden of a contralateral tumor, although additional studies would be necessary to elucidate this trend. The significant negative correlation between  $\text{AUC}_{\text{L/P}}$  and blood glucose, and similarly negative trend between  $k_{\text{PL}}$  and blood glucose, suggest that increased systemic availability of glucose leads to decreased conversion of lactate to pyruvate in these 4T07 and 4T1 tumors. It is therefore possible that glucose acts as a competitive substrate for energy metabolism, reducing uptake of hyperpolarized  $[1-^{13}\text{C}]$ pyruvate and, thereby, decreasing measures of pyruvate-to-lactate conversion. For example, previous work by Serrao et al. demonstrated lower variability in the measured hyperpolarized  $[1-^{13}\text{C}]$ lactate/ $[1-^{13}\text{C}]$ pyruvate ratio and  $k_{\text{PL}}$  in fasted animals where blood glucose levels are also expected to be more repeatable, indicating the influence of blood glucose on observed hyperpolarized  $[1-^{13}\text{C}]$ pyruvate metabolism [36].

## 4. Materials and Methods

### 4.1. Cell Culture

The 4T1 and 4T07 murine carcinoma cells used to generate orthotopic mammary tumors were purchased from American Type Culture Collection (ATCC). Cells were maintained in culture at 5%  $\text{CO}_2$  with RPMI 1640 plus 10% FCS. Prior to orthotopic injection the cells were lifted, washed 3 times in sterile PBS, counted, and resuspended in sterile PBS at a final concentration of  $1 \times 10^7$  per mL for 4T1s and  $2 \times 10^7$  for 4T07s.

### 4.2. Animal Model and Handling

All animal experiments complied with Institutional Animal Care and Use Committee guidelines and requirements. A cohort of 14 female BALB/c mice (mass = 19–31 g) were imaged. Mice were divided evenly for bilateral injection with 50  $\mu\text{L}$  of PBS containing either  $5 \times 10^5$  4T1 cells or  $1 \times 10^6$  4T07 murine breast cancer cells per inguinal mammary fat pad. These sample sizes were selected to approximately match those of Frees et al. who found a statistically significant difference in the delivery-corrected uptake of a fluorescent glucose derivative between these same orthotopic tumor models [23]. The 7 mice injected with 4T07 cells received 1 million cells per injection site except the first study which received  $\frac{1}{2}$  million cells per injection site. In all MRI experiments, 4T1 and 4T07 tumors were allowed to grow to a diameter of 0.5–1.0 cm. All mice were allowed unrestricted access to water but fasted for at least 4.5 h (mean  $\pm$  standard deviation (SD) fasting times of  $6.4 \pm 0.6$  h versus  $6.5 \pm 0.8$  h for 4T07 and 4T1 mice, respectively) prior to anesthetization to achieve more reproducible blood-glucose levels at the time of metabolic imaging [36].

Just before imaging, mice were anesthetized with 3% isoflurane in oxygen (1 L/min) and maintained at 1–2.5% isoflurane throughout imaging. A cannula was placed in the tail vein for intravenous injection of hyperpolarized  $[1-^{13}\text{C}]$ pyruvate during imaging. Internal body temperature and respiratory rate were continuously monitored using an intra-rectal fiber optic probe and respiratory pad, respectively. A warm air blower was placed approximately 5 cm from the tip of the mouse's tail to heat the animal to  $37 \pm 1$   $^\circ\text{C}$

during imaging. In a subset of 3 mice from each tumor line, a second hyperpolarized  $^{13}\text{C}$  MRSI study was performed 48 h after the initial experiment to assess repeatability of imaging measures of metabolism. The study design matrix is given in Table 4.

**Table 4.** Study design matrix.

Tumor Model	Total Mice Imaged	Subset of Mice with Repeat Study
4T07, dormant	7	3
4T1, metastatic	7	3
Total	14	6

#### 4.3. Biochemical and Immunohistochemical Analysis

Following each imaging study, and approximately 30 min after the hyperpolarized  $[1-^{13}\text{C}]$ pyruvate injection (i.e., the approximate time to complete the study),  $\sim 30\ \mu\text{L}$  of blood was drawn from the retro-orbital plexus while mice were still under anesthesia. Blood glucose and lactate levels were then measured using an Accu-Check Guide glucose meter (Roche, Basel, Switzerland) and a Lactate Plus lactate meter (Nova Biomedical, Waltham, MA, USA), respectively.

After the final imaging study, and following blood collection, mice were euthanized with  $\text{CO}_2$  and the tumors were harvested. Tumor length, width, and mass were recorded prior to any further tissue processing. Tumor volume was calculated from the length and width measurements [37]. Each tumor was divided for end-point analysis. For all mice except the first mouse bearing 4T07 tumors, one half of each tumor was snap frozen in liquid nitrogen and stored at  $-80\ ^\circ\text{C}$  for LDH activity analysis. The remaining tumor halves for all mice were fixed in formalin for 48 h and then switched to 70% ethanol for histopathology.

Tumor LDH activity was measured only for the targeted imaging tumor in each mouse. Furthermore, 16.5–28.0 mg of snap frozen tumor tissue in 825–1400  $\mu\text{L}$  of cold LDH assay buffer was homogenized on ice using an electric mixer. Samples were centrifuged at  $10,000\times g$  for 15 min at  $4\ ^\circ\text{C}$ . Moreover, 1  $\mu\text{L}$  of serum was then assayed for LDH activity (Sigma-Aldrich MAK066, St. Louis, MO, USA) at a dilution of 1:10. Samples were compared to a standard curve generated from 2.5–12.5 nmol of reduced nicotinamide adenine dinucleotide (NADH) standards run at 450 nm and  $37\ ^\circ\text{C}$ .

Formalin fixed paraffin embedded tissue was used for immunofluorescence analysis of LDHA (ThermoFisher, Waltham, MA, USA, 1:500 dilution), HIF-1 $\alpha$  (Invitrogen, Berlin, Germany, 1:200 dilution), MCT1 (ThermoFisher, Waltham, MA, USA, 1:400 dilution) and CD31 (Abcam, Cambridge, MA, USA, 1:100 dilution). Briefly, tumor sections were deparaffinized and rehydrated prior to antigen retrieval with citrate buffer [38]. Tissue was blocked for 1 h in 10% BSA (GeminiBio, West Sacramento, CA, USA) prior to incubation with primary antibody at room temperature. Tissue was then washed 3 times and incubated with the appropriate secondary antibody (Jackson Immuno Research, West Grove, PA USA, 1:500 dilution), counterstained with DAPI (ThermoFisher, Waltham, MA, USA), and mounted with ProLong Gold (ThermoFisher, Waltham, MA, USA).

The tumor sections were imaged using a  $20\times$  Nikon air objective on a Nikon inverted Ti-300 Epifluorescent Microscope. A minimum of 5 images per individual tissue section were collected by random sampling of the tumor section using SlideBook 6.0 acquisition software and further analyzed with ImageJ. For all antibodies except CD31, the mean intensity was calculated for each image with ImageJ. Outliers identified by ROUT (GraphPad, Prism v9.1.0) were removed prior to averaging the intensity from all fields of view per tumor to determine differences between 4T1 and 4T07 tumors. In the case of CD31, a threshold was applied to create a mask of CD31 area per field of view. The area per field of view (FOV) was then averaged for each tumor to identify differences in CD31 area in 4T1 vs. 4T07 tumors.

The following exclusion criteria were applied. Blood samples were processed incorrectly for biochemical analysis of serum lactate and glucose levels in the first 4T07 tumor-bearing mouse, leaving 19/20 total samples for analysis. Additionally, snap frozen tumor tissue was also collected incorrectly for biochemical analysis of tumor LDH in the first 4T07 tumor-bearing mouse, leaving 13/14 tumors for analysis; tumors were harvested and compared to the last imaging time point only.

#### 4.4. Hyperpolarization

Dynamic nuclear polarization (Hypersense, Tubney Woods, Abingdon, Oxfordshire, UK) was performed using 30  $\mu\text{L}$  aliquots of  $[1-^{13}\text{C}]$ pyruvic acid (Cambridge Isotope Laboratories Inc., Tewksbury, MA, USA) doped with 15 mM OX063 trityl radical (Oxford Instruments, Concord, MA, USA). Samples were irradiated with microwaves of 94.075 GHz and 100 mW to solid-state polarizations of over 98%. The sample was then rapidly dissolved in a 4-mL neutralizing solution of 128 mM NaOH, 140 mM Tris buffer, and 88 mg/L EDTA. A dose of 10  $\mu\text{L/g}$  of hyperpolarized sample was injected into the tail vein over 12–15 s during dynamic image acquisition. Liquid-state polarization of the remaining sample was measured in a bench-top polarimeter ( $^{13}\text{C}$ -MQC polarimeter, Oxford Instruments Molecular Biotech Ltd., Abingdon, Oxfordshire, UK), giving polarizations of  $18 \pm 3\%$  (mean  $\pm$  SD) at the time of injection. The final  $[1-^{13}\text{C}]$ pyruvate concentration and pH were  $\sim 110$  mM and  $7.8 \pm 0.2$  (mean  $\pm$  SD), respectively.

#### 4.5. Image Acquisition

All imaging was performed on a 4.7 T small animal MRI (Agilent, Palo Alto, CA, USA) using a dual-tuned  $^1\text{H}/^{13}\text{C}$  volume coil for  $^1\text{H}$  imaging and  $^{13}\text{C}$  excitation, and a  $^{13}\text{C}$  surface coil for signal reception (Doty Scientific, Columbia, SC, USA). The  $^{13}\text{C}$  surface coil was centered over one tumor to ensure relatively homogeneous signal reception in that tumor. The selected tumor was alternated between mice when possible, such that 8 right tumors and 6 left tumors were imaged across the 14 mice. Tumors were imaged when they measured 0.5–1.0 cm in diameter to minimize the chance of necrosis and ulceration.

Shimming was performed on the  $^1\text{H}$  channel and multi-echo,  $^1\text{H}$  spoiled-gradient echo (SPGR) data ( $\text{TR}/\text{TE}_1/\Delta\text{TE} = 34.0/4.2/0.4$  ms,  $\text{FOV} = 48 \times 48$  mm $^2$ , matrix =  $192 \times 192$ , slice thickness = 2 mm, flip angle =  $20^\circ$ , echoes = 8) were collected in order to generate a  $B_0$  field map using an image-space IDEAL reconstruction [39] for spatially-resolved frequency corrections in the direct IDEAL  $^{13}\text{C}$  reconstruction [40]. Additionally,  $^1\text{H}$ ,  $T_2$ -weighted fast spin-echo images ( $\text{FOV} = 48 \times 48$  mm $^2$ , matrix =  $192 \times 192$ , slice thickness = 2 mm,  $\text{TR}/\text{TE}_{\text{eff}} = 3500/66$  ms, echo-train length = 8) were acquired for anatomical reference.

For  $^{13}\text{C}$  MRSI, power and frequency calibrations were performed with a thermally polarized phantom of 9.4 M  $^{13}\text{C}$ -urea (Cambridge Isotope Laboratories Inc., Tewksbury, MA, USA) doped with 8.5 mM gadobenate dimeglumine (Bracco Diagnostics, Inc., Princeton, NJ, USA) placed in the imaging field of view (FOV). Approximately 20 s prior to injection of hyperpolarized  $[1-^{13}\text{C}]$ pyruvate, dynamic, constant-density, k-t spiral acquisitions were started with the following parameters:  $\text{TR}/\text{TE}_1 = 50\text{--}150/0.318$  ms,  $\text{NE} = 6$ , flip angle =  $10^\circ$ , and receiver bandwidth = 250 kHz. To achieve 1–3 pixels per tumor diameter, the nominal in-plane resolution was  $3 \times 3$  mm $^2$  (i.e., nominal  $\text{FOV} = 48 \times 48$  mm $^2$  and nominal matrix =  $16 \times 16$ ) and the slice thickness was 5 mm. A FOV-oversampling factor of  $\eta = 7$  was used, resulting in a prescribed FOV and matrix of  $336 \times 336$  mm $^2$  and  $112 \times 112$ , respectively. For all  $^{13}\text{C}$  spiral acquisitions, the maximum gradient slew rate was derated to maintain a 30 ms readout for high acquisition SNR efficiency [41] assuming a realistic  $T_2^*$  [42–44]. Slice-selective spectra (flip angle =  $5^\circ$ , receiver bandwidth = 5 kHz) were interleaved between  $^{13}\text{C}$  image acquisitions to guide selection of metabolite peak frequencies in the direct IDEAL reconstruction. In total, 32 time frames were acquired at  $\sim 5$  s temporal resolution following each injection.

#### 4.6. Image Reconstruction

Metabolite images of hyperpolarized [1-<sup>13</sup>C]pyruvate, [1-<sup>13</sup>C]lactate, [1-<sup>13</sup>C]alanine, [1-<sup>13</sup>C]pyruvate-hydrate, and thermally-polarized <sup>13</sup>C-urea were reconstructed using a direct IDEAL reconstruction in MATLAB (R2015b, The MathWorks, Natick, MA, USA) interfacing with C++. Reconstructions incorporated the estimated <sup>1</sup>H B<sub>0</sub> field maps, divided by a factor of four to account for the difference in <sup>1</sup>H and <sup>13</sup>C gyromagnetic ratios [40]. Gradient trajectory imperfections were also corrected using a thin slice-based technique [45]. Metabolite peak frequencies used in the reconstruction were identified as follows.

The relative offset of the excitation center frequency from [1-<sup>13</sup>C]pyruvate is difficult to decouple from B<sub>0</sub> inhomogeneities influencing the hyperpolarized <sup>13</sup>C slice-selective spectra. To resolve these two sources of off-resonance, the image of <sup>13</sup>C metabolism was compared with the <sup>1</sup>H SPGR anatomical image using mutual information while varying the chemical shift of [1-<sup>13</sup>C]pyruvate and [1-<sup>13</sup>C]lactate at 4.7 T to be 614 ± 20 Hz using an exhaustive search. The frequency combination used in the final reconstruction of all 32 <sup>13</sup>C imaging time frames was the one that maximized the mutual information between the anatomy and the [1-<sup>13</sup>C]pyruvate and [1-<sup>13</sup>C]lactate that fell within the specified 614 ± 20 Hz range. [1-<sup>13</sup>C]alanine, [1-<sup>13</sup>C]pyruvate-hydrate, and <sup>13</sup>C-urea were assumed to be at their known chemical shifts relative to [1-<sup>13</sup>C]pyruvate at 4.7 T (i.e., 433 Hz, 272 Hz, and −366 Hz from the [1-<sup>13</sup>C]pyruvate frequency, respectively).

#### 4.7. Image Analysis

All image analysis was performed in MATLAB (R2015b, The MathWorks, Natick, MA, USA). Dynamic images of metabolism were first baseline corrected by subtracting the mean signal from time frames prior to hyperpolarized [1-<sup>13</sup>C]pyruvate injection. Voxel-wise area-under-the-curve ratios of lactate-to-pyruvate (AUC<sub>L/P</sub>) were then calculated [16] and the mean AUC<sub>L/P</sub> for each tumor was found using a manually segmented region of interest (ROI) from a single individual. These same ROIs were used to calculate the mean hyperpolarized [1-<sup>13</sup>C]pyruvate and [1-<sup>13</sup>C]lactate signals in each tumor for each time frame. The resulting metabolite time courses were also fit to the two-way exchange model with a Heaviside step function to incorporate pyruvate inflow [25] in order to estimate the apparent exchange rate of pyruvate-to-lactate (k<sub>PL</sub>). For the first 4T1 tumor-bearing mouse, <sup>13</sup>C MRSI metabolite time courses lacked sufficient SNR for kinetic modeling to estimate k<sub>PL</sub>, resulting in k<sub>PL</sub> being estimated for 19/20 total imaging experiments. Due to the insufficient metabolite SNR in the contralateral tumors for reliable kinetic modeling, and the variability in positioning of the contralateral tumors with respect to the <sup>13</sup>C surface-receive coil, imaging measures of metabolism are only presented for the primary tumors. Additionally, [1-<sup>13</sup>C]alanine and [1-<sup>13</sup>C]pyruvate-hydrate tumor signals were at or near the level of the noise in the metabolite images and, therefore, were not analyzed in this work.

#### 4.8. Statistical Analysis

All statistical tests were performed in R 3.5.0 [46] unless otherwise stated. Unpaired, two-tailed *t*-tests were used to assess differences in k<sub>PL</sub>, AUC<sub>L/P</sub>, tumor LDH activity, and blood lactate and glucose levels between metastatic 4T1 and metastatic dormant 4T07 tumor models. For IHC, statistical analysis was performed using GraphPad Prism V6 (GraphPad Software, San Diego, CA, USA). A Shapiro–Wilk test for normality was performed, followed by Mann–Whitney test for normal data, or an unpaired *t*-test when data failed the normality test. Only imaging and biochemical metabolic markers from the first imaging day were used when comparing the two tumor models whereas immunohistochemistry stains were only available from the last imaging time point for each mouse. All available data from 4T1 and 4T07 tumor models on all imaging days were combined for correlation analysis. A non-parametric Spearman correlation test was used to compare the imaging metrics, k<sub>PL</sub> and AUC<sub>L/P</sub>, with the following biochemical and IHC markers: tumor LDH activity, blood lactate and glucose levels, and tissue expression of LDHA, MCT1, HIF-1α, and CD31. Additionally, since AUC<sub>L/P</sub> is meant to be a model-free

parameter proportional to  $k_{PL}$ , the correlation between  $AUC_{L/P}$  and  $k_{PL}$  was also tested. Imaging metrics and biochemical and IHC markers were also tested for correlation with tumor volume. Lastly, a correlation test was performed between tumor LDH activity and tumor LDHA expression. Results were considered significant for  $\alpha \leq 0.05$ .

## 5. Conclusions

Consistent with in vitro studies, hyperpolarized  $[1-^{13}C]$ pyruvate MRSI measures of in vivo glycolytic flux, namely,  $k_{PL}$  and  $AUC_{L/P}$ , exhibited an increasing trend between metastatic dormant (4T07) and highly metastatic (4T1) murine breast cancer models, although differences were not statistically significant. Importantly, a significant positive correlation was found between  $AUC_{L/P}$  and tumor LDH activity, further supporting  $AUC_{L/P}$  as a biomarker of in vivo glycolytic pyruvate-to-lactate conversion rate. IHC showed that MCT1 and LDHA did not correlate with  $k_{PL}$  and  $AUC_{L/P}$ , suggesting  $[1-^{13}C]$ pyruvate MRSI is mostly driven by LDH enzyme activity in this model.

**Author Contributions:** Conceptualization, S.B.F., S.M.P., K.W.E., R.M.S., S.E.-B. and E.B.M.; methodology, S.B.F., E.B.M., G.P.B., S.M.P., S.E.-B., D.R.I. and P.B.; software, E.B.M.; validation, E.B.M., G.P.B., S.E.-B. and B.L.C.; formal analysis, E.B.M., G.P.B., S.M.P., S.B.F. and P.B.; investigation, E.B.M., G.P.B., S.E.-B., D.R.I. and S.M.P.; resources, S.B.F. and S.M.P.; data curation, S.B.F., E.B.M., G.P.B., P.B. and S.M.P.; writing—original draft preparation, E.B.M.; writing—review and editing, S.B.F., E.B.M., P.B., S.M.P., G.P.B., S.E.-B., D.R.I., K.W.E., B.L.C. and R.M.S.; visualization, S.B.F., E.B.M. and P.B.; supervision, S.B.F. and S.M.P.; project administration, S.B.F., S.M.P. and K.W.E.; funding acquisition, S.B.F., S.M.P., K.W.E. and R.M.S. All authors have read and agreed to the published version of the manuscript.

**Funding:** This project was supported in part by the AAPM 2014 Graduate Fellowship, the Department of Medical Physics at the University of Wisconsin-Madison, NIH/NIDDK R01 DK092454, grant UL1TR000427 to UW ICTR from NIH/NCATS, GE Healthcare, UW Carbone Cancer Comprehensive Cancer Center CCSG P30CA014520, and the Radiological Society of North America Research and Education Foundation. GB was supported by the National Institute of Allergy and Immunological Diseases under award number T32AI007635. PB was supported by a radiological sciences training grant T32 CA009206 fellowship.

**Institutional Review Board Statement:** The study was conducted according to the Guidelines for Ethical Conduct in the Care and Use of Animals, and approved by the Institutional Animal Care and Use Committee of the University of Wisconsin-Madison (protocol code M005500-R01, approved on 24 June 2019).

**Informed Consent Statement:** Not applicable.

**Data Availability Statement:** Data are available in a publicly accessible repository at: <https://www.medphysics.wisc.edu/research/pulmonary-imaging/>. Please contact the corresponding author for further details.

**Conflicts of Interest:** SBF receives research support from GE Healthcare for the development of hyperpolarized MRI.

## Appendix A

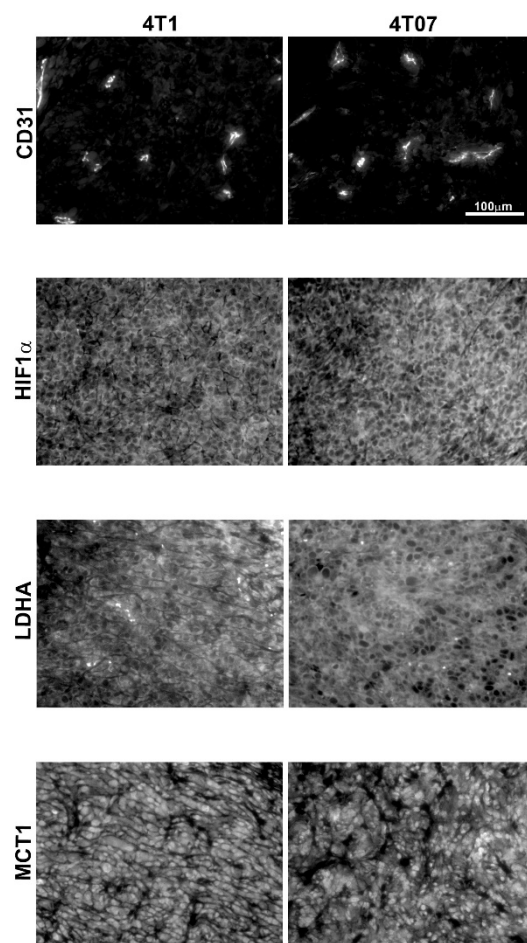


**Figure A1.** Representative images of CD31, HIF-1 $\alpha$ , LDHA, and MCT1 immunofluorescence in 4T1 vs. 4T07 tumors.

## Appendix B

### Appendix B.1. Correlation of Imaging Measures of Metabolism

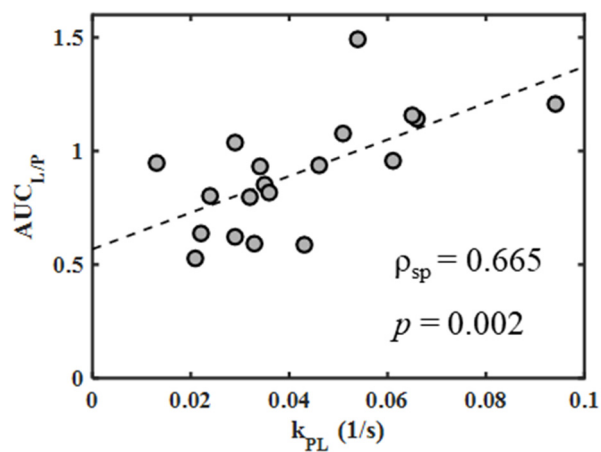


**Figure A2.** Spearman correlation plot comparing  $AUC_{L/P}$  with  $k_{PL}$ . The Spearman correlation coefficient ( $\rho_{sp}$ ) and  $p$ -value are listed on the plot.

## Appendix B.2. Repeatability of Metabolic Measures

### Appendix B.2.1. Methods

In a subset of 3 mice from each tumor line, a second hyperpolarized  $^{13}\text{C}$  MRSI study was performed 48 h after the initial experiment to assess repeatability of imaging measures of metabolism. For measures of repeatability, imaging metrics and blood metabolite levels from mice with 4T1 and 4T07 tumors were combined for a total of six paired measurements for each repeated metabolic metric. Bland–Altman plots were created in MATLAB (R2015b, The MathWorks, Natick, MA, USA) to assess limits of agreement and bias of repeated measures while paired t-tests were used to test for differences in repeated measures between the two imaging days.

### Appendix B.2.2. Results

Bland–Altman plots for repeated imaging and biochemical metabolic measures (Figure A3) display limits of agreement on the order of the mean measurement values for  $k_{\text{PL}}$ ,  $\text{AUC}_{\text{L/P}}$ , and blood glucose levels, indicating the variability in repeat testing in the same animal was at the same order of magnitude as the variability between mice. Blood lactate levels, however, displayed smaller relative limits of agreement than the other metabolic measures, indicating better test-retest repeatability. None of the repeated metabolic measures were found to be significantly different between repeat studies (Table A1). Blood glucose levels displayed a trend of decreasing between the first and second studies ( $p = 0.21$ ) as is reflected in the positive bias on the Bland–Altman plot. No other measures, including imaging measures of the conversion rate of pyruvate-to-lactate (i.e.,  $k_{\text{PL}}$  and  $\text{AUC}_{\text{L/P}}$ ), displayed systematic biases in pyruvate-to-lactate for the second imaging time point compared to the first.

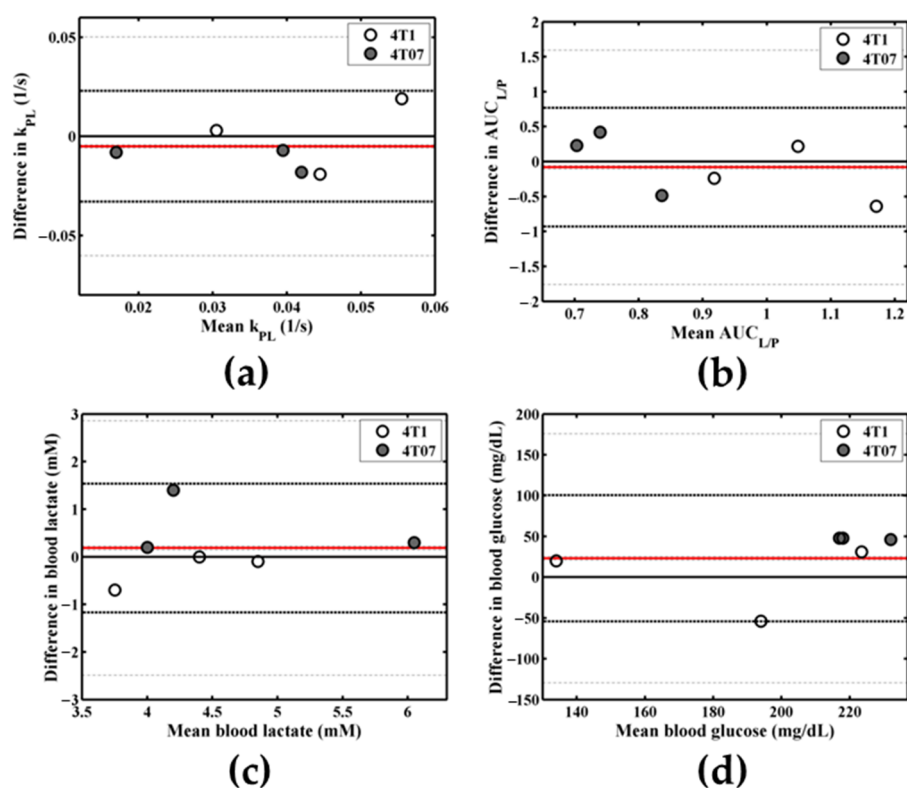


**Figure A3.** Bland–Altman repeatability plots for  $k_{\text{PL}}$  (a),  $\text{AUC}_{\text{L/P}}$  (b), blood lactate level (c), and blood glucose level (d) including the limits of agreement (dashed black lines), 95% confidence intervals for the limits of agreement (dash-dot gray lines), and bias (solid red line).

**Table A1.** Summary of repeated measure results for combined data from 4T07 and 4T1 tumor models. Mean values  $\pm$  standard deviations (SD), paired *t*-test results, and Bland–Altman limits of agreement (LOA), 95% confidence intervals (CI), and bias are included. Each imaging and biochemical metric included 6 paired samples (i.e., 3, 4T1 and 3, 4T07 samples combined).

Metabolic Measure	Day 1 Mean $\pm$ SD	Day 2 Mean $\pm$ SD	<i>p</i> -Value	Lower LOA (95% CI)	Upper LOA (95% CI)	Bias	COV
$k_{PL}$ (1/s)	0.036 $\pm$ 0.017	0.041 $\pm$ 0.013	0.43	−0.03 (−0.06, −0.01)	0.02 (0.00, 0.05)	−0.01	0.23
AUC <sub>L/P</sub>	0.86 $\pm$ 0.19	0.94 $\pm$ 0.35	0.66	−0.93 (−1.76, −0.10)	0.77 (−0.06, 1.59)	−0.08	0.29
Blood lactate (mM)	4.6 $\pm$ 0.9	4.5 $\pm$ 0.9	0.54	−1.17 (−2.49, 0.15)	1.54 (0.22, 2.86)	0.18	0.08
Blood glucose (mg/dL)	215 $\pm$ 47	192 $\pm$ 35	0.21	−54 (−129, 21)	100 (25, 176)	23	0.14

### Appendix B.2.3. Discussion

The test-retest repeatability of AUC<sub>L/P</sub> and  $k_{PL}$ , as well as blood glucose and lactate levels all exhibited Bland–Altman limits of agreement with magnitudes on the order of the mean measurement value, indicating that test-retest variability in the same animal was in the same order as variability between animals. This wide variability was likely due, at least in part, to the 48 h window between repeat studies. This window was intended to give each mouse's systemic physiology time to renormalize following imaging studies which involved fasting for over 5 h, anesthetization with isoflurane for at least 1 h, a supraphysiologic injection of [1-<sup>13</sup>C]pyruvate, and a retro-orbital blood draw of approximately 1–2% of the total blood volume. However, given the rapid growth rates of the 4T07 and 4T1 tumors, it is likely possible that the tumor microenvironment also changed in this time frame. Furthermore, AUC<sub>L/P</sub> and  $k_{PL}$  were found to correlate positively ( $p = 0.002$ ), in line with previous results [19] and further demonstrates the accuracy of the lactate quantification as obtained through hyperpolarized <sup>13</sup>C MRSI acquired in this study.

### References

1. American Cancer Society. *Global Cancer Facts & Figures*, 3rd ed.; American Cancer Society: Atlanta, GA, USA, 2015.
2. Linde, N.; Fluegen, G.; Aguirre-Ghiso, J.A. The relationship between dormant cancer cells and their microenvironment. *Adv. Cancer Res.* **2016**, *132*, 45–71. [[PubMed](#)]
3. Hanahan, D.; Weinberg, R.A. Hallmarks of cancer: The next generation. *Cell* **2011**, *144*, 646–674. [[CrossRef](#)] [[PubMed](#)]
4. Vander Heiden, M.G.; Cantley, L.C.; Thompson, C.B. Understanding the warburg effect: The metabolic requirements of cell proliferation. *Science* **2009**, *324*, 1029–1033. [[CrossRef](#)]
5. Hirschhaeuser, F.; Sattler, U.G.; Mueller-Klieser, W. Lactate: A metabolic key player in cancer. *Cancer Res.* **2011**, *71*, 6921–6925. [[CrossRef](#)]
6. Ardenkjaer-Larsen, J.H.; Fridlund, B.; Gram, A.; Hansson, G.; Hansson, L.; Lerche, M.H.; Servin, R.; Thaning, M.; Golman, K. Increase in signal-to-noise ratio of > 10,000 times in liquid-state nmr. *Proc. Natl. Acad. Sci. USA* **2003**, *100*, 10158–10163. [[CrossRef](#)] [[PubMed](#)]
7. Day, S.E.; Kettunen, M.I.; Gallagher, F.A.; Hu, D.E.; Lerche, M.; Wolber, J.; Golman, K.; Ardenkjaer-Larsen, J.H.; Brindle, K.M. Detecting tumor response to treatment using hyperpolarized <sup>13</sup>c magnetic resonance imaging and spectroscopy. *Nat. Med.* **2007**, *13*, 1382–1387. [[CrossRef](#)] [[PubMed](#)]
8. Chen, A.P.; Albers, M.J.; Cunningham, C.H.; Kohler, S.J.; Yen, Y.F.; Hurd, R.E.; Tropp, J.; Bok, R.; Pauly, J.M.; Nelson, S.J.; et al. Hyperpolarized c-13 spectroscopic imaging of the tramp mouse at 3t—initial experience. *Magn. Reson. Med.* **2007**, *58*, 1099–1106. [[CrossRef](#)]
9. Xu, H.N.; Kadlenceck, S.; Profka, H.; Glickson, J.D.; Rizi, R.; Li, L.Z. Is higher lactate an indicator of tumor metastatic risk? A pilot mrs study using hyperpolarized <sup>13</sup>c-pyruvate. *Acad. Radiol.* **2014**, *21*, 223–231. [[CrossRef](#)]
10. Xu, H.N.; Kadlenceck, S.; Pullinger, B.; Profka, H.; Cai, K.; Hariharan, H.; Rizi, R.; Li, L.Z. In vivo metabolic evaluation of breast tumor mouse xenografts for predicting aggressiveness using the hyperpolarized <sup>13</sup>c-nmr technique. *Adv. Exp. Med. Biol.* **2013**, *789*, 237–242.
11. Ward, C.S.; Venkatesh, H.S.; Chaumeil, M.M.; Brandes, A.H.; Vancricking, M.; Dafni, H.; Sukumar, S.; Nelson, S.J.; Vigneron, D.B.; Kurhanewicz, J.; et al. Noninvasive detection of target modulation following phosphatidylinositol 3-kinase inhibition using hyperpolarized <sup>13</sup>c magnetic resonance spectroscopy. *Cancer Res.* **2010**, *70*, 1296–1305. [[CrossRef](#)] [[PubMed](#)]
12. Shin, P.J.; Zhu, Z.; Camarda, R.; Bok, R.A.; Zhou, A.Y.; Kurhanewicz, J.; Goga, A.; Vigneron, D.B. Cancer recurrence monitoring using hyperpolarized [1-<sup>13</sup>c]pyruvate metabolic imaging in murine breast cancer model. *Magn. Reson. Imaging* **2017**, *43*, 105–109. [[CrossRef](#)]

13. Granlund, K.L.; Morris, E.A.; Vargas, H.A.; Lyashchenko, S.K.; DeNoble, P.J.; Sacchini, V.A.; Sosa, R.A.; Kennedy, M.A.; Nicholson, D.; Guo, Y.; et al. First-in-Woman Study of in Vivo Breast Cancer Metabolism Using Hyperpolarized [1-<sup>13</sup>C] Pyruvate. In Proceedings of the 24th Annual Meeting of ISMRM, Singapore, 7–13 May 2016.
14. Harper, K.L.; Sosa, M.S.; Entenberg, D.; Hosseini, H.; Cheung, J.F.; Nobre, R.; Avivar-Valderas, A.; Nagi, C.; Girmius, N.; Davis, R.J.; et al. Mechanism of early dissemination and metastasis in her2. *Nature* **2016**, *540*, 588–592. [[CrossRef](#)]
15. Morris, B.A.; Burkel, B.; Ponik, S.M.; Fan, J.; Condeelis, J.S.; Aguirre-Ghiso, J.A.; Castracane, J.; Denu, J.M.; Keely, P.J. Collagen matrix density drives the metabolic shift in breast cancer cells. *EBioMedicine* **2016**, *13*, 146–156. [[CrossRef](#)] [[PubMed](#)]
16. Hill, D.K.; Orton, M.R.; Mariotti, E.; Boulton, J.K.; Panek, R.; Jafar, M.; Parkes, H.G.; Jamin, Y.; Miniotti, M.F.; Al-Saffar, N.M.; et al. Model free approach to kinetic analysis of real-time hyperpolarized <sup>13</sup>C magnetic resonance spectroscopy data. *PLoS ONE* **2013**, *8*, e71996. [[CrossRef](#)] [[PubMed](#)]
17. Bonuccelli, G.; Tsirigos, A.; Whitaker-Menezes, D.; Pavlides, S.; Pestell, R.G.; Chiavarina, B.; Frank, P.G.; Flomenberg, N.; Howell, A.; Martinez-Outschoorn, U.E.; et al. Ketones and lactate “Fuel” Tumor growth and metastasis: Evidence that epithelial cancer cells use oxidative mitochondrial metabolism. *Cell Cycle (Georget. Tex.)* **2010**, *9*, 3506–3514. [[CrossRef](#)]
18. DeBerardinis, R.J.; Chandel, N.S. Fundamentals of cancer metabolism. *Sci. Adv.* **2016**, *2*, e1600200. [[CrossRef](#)]
19. Gallagher, F.A.; Woitek, R.; McLean, M.A.; Gill, A.B.; Manzano Garcia, R.; Provenzano, E.; Riemer, F.; Kaggie, J.; Chhabra, A.; Ursprung, S.; et al. Imaging breast cancer using hyperpolarized carbon-13 mri. *Proc. Natl. Acad. Sci. USA* **2020**, *117*, 2092–2098. [[CrossRef](#)]
20. Lau, J.Y.; Chen, A.P.; Gu, Y.P.; Cunningham, C.H. Voxel-by-voxel correlations of perfusion, substrate, and metabolite signals in dynamic hyperpolarized <sup>13</sup>C imaging. *NMR Biomed.* **2016**, *29*, 1038–1047. [[CrossRef](#)]
21. Kettunen, M.I.; Hu, D.E.; Witney, T.H.; McLaughlin, R.; Gallagher, F.A.; Bohndiek, S.E.; Day, S.E.; Brindle, K.M. Magnetization transfer measurements of exchange between hyperpolarized [1-<sup>13</sup>C]pyruvate and [1-<sup>13</sup>C]lactate in a murine lymphoma. *Magn. Reson. Med.* **2010**, *63*, 872–880. [[CrossRef](#)] [[PubMed](#)]
22. Fan, J.; Hitosugi, T.; Chung, T.W.; Xie, J.; Ge, Q.; Gu, T.L.; Polakiewicz, R.D.; Chen, G.Z.; Boggon, T.J.; Lonial, S.; et al. Tyrosine phosphorylation of lactate dehydrogenase is important for nadh/nad(+) redox homeostasis in cancer cells. *Mol. Cell Biol.* **2011**, *31*, 4938–4950. [[CrossRef](#)]
23. Frees, A.E.; Rajaram, N.; McCachren, S.S., III; Fontanella, A.N.; Dewhurst, M.W.; Ramanujam, N. Delivery-corrected imaging of fluorescently-labeled glucose reveals distinct metabolic phenotypes in murine breast cancer. *PLoS ONE* **2014**, *9*, e115529. [[CrossRef](#)]
24. Harris, T.; Eliyahu, G.; Frydman, L.; Degani, H. Kinetics of hyperpolarized <sup>13</sup>C<sub>1</sub>-pyruvate transport and metabolism in living human breast cancer cells. *Proc. Natl. Acad. Sci. USA* **2009**, *106*, 18131–18136. [[CrossRef](#)]
25. Daniels, C.J.; McLean, M.A.; Schulte, R.F.; Robb, F.J.; Gill, A.B.; McGlashan, N.; Graves, M.J.; Schwaiger, M.; Lomas, D.J.; Brindle, K.M.; et al. A comparison of quantitative methods for clinical imaging with hyperpolarized <sup>13</sup>C-pyruvate. *NMR Biomed.* **2016**, *29*, 387–399. [[CrossRef](#)]
26. Gupta, S.; Roy, A.; Dwarakanath, B.S. Metabolic cooperation and competition in the tumor microenvironment: Implications for therapy. *Front. Oncol.* **2017**, *7*, 68. [[CrossRef](#)]
27. Sotgia, F.; Martinez-Outschoorn, U.E.; Pavlides, S.; Howell, A.; Pestell, R.G.; Lisanti, M.P. Understanding the warburg effect and the prognostic value of stromal caveolin-1 as a marker of a lethal tumor microenvironment. *Breast Cancer Res. BCR* **2011**, *13*, 213. [[CrossRef](#)]
28. Xu, H.N.; Nioka, S.; Glickson, J.D.; Chance, B.; Li, L.Z. Quantitative mitochondrial redox imaging of breast cancer metastatic potential. *J. Biomed. Opt.* **2010**, *15*, 036010. [[CrossRef](#)]
29. Chen, A.P.; Hurd, R.E.; Schroeder, M.A.; Lau, A.Z.; Gu, Y.P.; Lam, W.W.; Barry, J.; Tropp, J.; Cunningham, C.H. Simultaneous investigation of cardiac pyruvate dehydrogenase flux, krebs cycle metabolism and ph, using hyperpolarized [1,2-<sup>13</sup>C<sub>2</sub>]pyruvate in vivo. *NMR Biomed.* **2012**, *25*, 305–311. [[CrossRef](#)] [[PubMed](#)]
30. Hu, S.; Yoshihara, H.A.; Bok, R.; Zhou, J.; Zhu, M.; Kurhanewicz, J.; Vigneron, D.B. Use of hyperpolarized [1-<sup>13</sup>C]pyruvate and [2-<sup>13</sup>C]pyruvate to probe the effects of the anticancer agent dichloroacetate on mitochondrial metabolism in vivo in the normal rat. *Magn. Reson. Imaging* **2012**, *30*, 1367–1372. [[CrossRef](#)] [[PubMed](#)]
31. Qu, W.; Zha, Z.; Lieberman, B.P.; Mancuso, A.; Stetz, M.; Rizzi, R.; Ploessl, K.; Wise, D.; Thompson, C.; Kung, H.F. Facile synthesis [5-<sup>13</sup>C-4-<sup>2</sup>H<sub>2</sub>]-l-glutamine for hyperpolarized mrs imaging of cancer cell metabolism. *Acad. Radiol.* **2011**, *18*, 932–939. [[CrossRef](#)]
32. Hou, Y.; Zhou, M.; Xie, J.; Chao, P.; Feng, Q.; Wu, J. High glucose levels promote the proliferation of breast cancer cells through gtpases. *Breast Cancer (Dove Med. Press)* **2017**, *9*, 429–436. [[CrossRef](#)] [[PubMed](#)]
33. Haseen, S.D.; Khanam, A.; Sultan, N.; Idrees, F.; Akhtar, N.; Imtiaz, F. Elevated fasting blood glucose is associated with increased risk of breast cancer: Outcome of case-control study conducted in karachi, pakistan. *Asian Pac. J. Cancer Prev. APJCP* **2015**, *16*, 675–678. [[CrossRef](#)]
34. Shapot, V.S.; Blinov, V.A. Blood glucose levels and gluconeogenesis in animals bearing transplantable tumors. *Cancer Res.* **1974**, *34*, 1827–1832.
35. Svaninger, G.; Drott, C.; Lundholm, K. Role of insulin in development of cancer cachexia in nongrowing sarcoma-bearing mice: Special reference to muscle wasting. *J. Natl. Cancer Inst.* **1987**, *78*, 943–950.

36. Serrao, E.M.; Rodrigues, T.B.; Gallagher, F.A.; Kettunen, M.I.; Kennedy, B.W.C.; Vowler, S.L.; Burling, K.A.; Brindle, K.M. Effects of fasting on serial measurements of hyperpolarized [1-<sup>13</sup>C]pyruvate metabolism in tumors. *NMR Biomed.* **2016**, *29*, 1048–1055. [[CrossRef](#)]
37. Faustino-Rocha, A.; Oliveira, P.A.; Pinho-Oliveira, J.; Teixeira-Guedes, C.; Soares-Maia, R.; da Costa, R.G.; Colaco, B.; Pires, M.J.; Colaco, J.; Ferreira, R.; et al. Estimation of rat mammary tumor volume using caliper and ultrasonography measurements. *Lab Anim.* **2013**, *42*, 217–224. [[CrossRef](#)]
38. Esbona, K.; Inman, D.; Saha, S.; Jeffery, J.; Schedin, P.; Wilke, L.; Keely, P. Cox-2 modulates mammary tumor progression in response to collagen density. *Breast Cancer Res.* **2016**, *18*, 35. [[CrossRef](#)]
39. Hernando, D.; Kellman, P.; Haldar, J.P.; Liang, Z.P. Robust water/fat separation in the presence of large field inhomogeneities using a graph cut algorithm. *Magn. Reson. Med.* **2010**, *63*, 79–90. [[CrossRef](#)] [[PubMed](#)]
40. Gordon, J.W.; Niles, D.J.; Fain, S.B.; Johnson, K.M. Joint spatial-spectral reconstruction and k-t spirals for accelerated 2d spatial/1d spectral imaging of <sup>13</sup>C dynamics. *Magn. Reson. Med.* **2014**, *71*, 1435–1445. [[CrossRef](#)]
41. Qin, Q. Point spread functions of the t<sub>2</sub> decay in k-space trajectories with long echo train. *Magn. Reson. Imaging* **2012**, *30*, 1134–1142. [[CrossRef](#)]
42. Wiesinger, F.; Weidl, E.; Menzel, M.I.; Janich, M.A.; Khagai, O.; Glaser, S.J.; Haase, A.; Schwaiger, M.; Schulte, R.F. Ideal spiral csi for dynamic metabolic mr imaging of hyperpolarized [1-<sup>13</sup>C]pyruvate. *Magn. Reson. Med.* **2012**, *68*, 8–16. [[CrossRef](#)]
43. Gordon, J.W.; Niles, D.J.; Adamson, E.B.; Johnson, K.M.; Fain, S.B. Application of flow sensitive gradients for improved measures of metabolism using hyperpolarized <sup>13</sup>C mri. *Magn. Reson. Med.* **2016**, *75*, 1242–1248. [[CrossRef](#)]
44. Durst, M.; Koellisch, U.; Frank, A.; Rancan, G.; Gringeri, C.V.; Karas, V.; Wiesinger, F.; Menzel, M.I.; Schwaiger, M.; Haase, A.; et al. Comparison of acquisition schemes for hyperpolarised <sup>13</sup>C imaging. *NMR Biomed.* **2015**, *28*, 715–725. [[CrossRef](#)]
45. Duyn, J.H.; Yang, Y.; Frank, J.A.; van der Veen, J.W. Simple correction method for k-space trajectory deviations in mri. *J. Magn. Reson.* **1998**, *132*, 150–153. [[CrossRef](#)] [[PubMed](#)]
46. R Core Team. *R: A language and Environment for Statistical Computing*; R Foundation for Statistical Computing: Vienna, Austria, 2018.